Journal of Zhejiang University-SCIENCE A 2026 27(4):384-399
www.jzus.zju.edu.cn; www.springer.com/journal/11582
E-mail: jzus_a@zju.edu.cn

Research Article

https://doi.org/10.1631/jzus.A2500194

Effect of laminar plasma quenching technology on the anti-wear and anti-fatigue properties of two types of U75V rail welded joints

Jingmang XU[1,2*✉], Hui ZHU[1,2*], Wenfeng GAO[1,2], Taoshuo BAI[1,2], Jian YANG[1,2], Kai WANG[3✉], Yao QIAN[1,2], Ping WANG[1,2]

[1] *MOE Key Laboratory of High-speed Railway Engineering, Southwest Jiaotong University, Chengdu 610031, China*
[2] *School of Civil Engineering, Southwest Jiaotong University, Chengdu 610031, China*
[3] *College of Design and Engineering, National University of Singapore, Singapore 117356, Singapore*

Abstract: The performance of rail welded joints significantly affects the safety of railways. In this study, we compare the fatigue damage of U75V thermite welded joints (TWJs) and flash-butt welded joints (FWJs), and subsequently explore the effect of laminar plasma quenching (LPQ) on the anti-wear and anti-fatigue properties of these two types of joints. The results indicate that LPQ reduced the wear of the FWJs by 78%–85%. Crack propagation in quenched thermite welded joints (QTJs) is observed to be controlled by the subsurface defect-initiated crack (SDIC) mechanism, whereas the crack propagation in quenched flash-butt welded joints (QFJs) involves two mechanisms: surface-originated fatigue crack (SOFC) and SDIC. Elemental fluctuations and changes in dislocation density account for the differences in wear mechanisms and fatigue damage between these two forms of quenched welded joints.

Key words: Laminar plasma quenching (LPQ) technology; Rail welded joints; Rolling contact fatigue (RCF); Wear

1 Introduction

With the rapid development of the railway transportation industry toward higher speeds and heavier loads, there is an increasing focus on the safety and reliability of steel rails. Over the long-term operation of railway systems, rail materials are subjected to the combined effects of environmental conditions and train loads, as well as the interactions of multiple physical factors. This results in significant wear and rolling contact fatigue (RCF) damage to the rail surface (Zeng et al., 2017). The presence of fatigue cracks, excessive wear, and large-scale spalling on the surface of steel rails poses a serious threat to the stability and safety of train operations, and escalates the costs and difficulties of track maintenance (Nejad et al., 2016; Seo et al., 2016).

Since rail welded joints are critical components that connect rails and ensure smooth train operations, their wear resistance and RCF resistance are essential. However, compared to rail substrates, the microstructure of rail welded joints is more complex. Additionally, the large residual stresses and defects generated during the welding process make the welded joint more susceptible to fatigue cracks during service (Remes et al., 2020; Fang et al., 2022). This increased risk of fatigue crack initiation and propagation poses a significant challenge to the reliability of rails (Hultgren et al., 2023; Li et al., 2025). According to relevant standards, joint performance can be enhanced by optimizing welding process parameters, improving the sequence and direction of welding, and employing techniques such as vibration aging. However, studies have demonstrated that these methods have certain limitations that cannot completely eliminate residual stresses and defects in welded joints. Additionally, their effectiveness is constrained by process conditions and material properties (Ghazanfari and Tehrani, 2021).

✉ Jingmang XU, mang080887@163.com
Kai WANG, wangkai@nus.edu.sg

[*] The two authors contributed equally to this work

Jingmang XU, https://orcid.org/0000-0003-3240-8652
Hui ZHU, https://orcid.org/0009-0005-8498-803X

Received May 15, 2025; Revision accepted Nov. 7, 2025;
Crosschecked Jan. 21, 2026; Online first Mar. 25, 2026

Additionally, surface strengthening techniques can be utilized to enhance wear resistance, mitigate fatigue damage, and improve the overall quality of rail welded joints. For instance, Hernández et al. (2016) used laser cladding to minimize plastic deformation in the heat affected (HA) zone of thermite welded joints (TWJs). Shi et al. (2019) investigated the effect of two laser strengthening techniques—laser quenching (LQ) and laser shock peening (LSP)—on the wear and fatigue resistance of U75V steel flash-butt welded heads through RCF tests. Moreover, Liu et al. (2019) used laser shock peening to strengthen the surface properties of friction stir welding joints for aluminum alloys. Li et al. (2022) analyzed the effect of LSP treatment on the fatigue resistance of U75VG steel flash-butt welded joints (FWJs) by investigating changes in the distribution of residual stress, microstructures, and surface morphology. Tan et al. (2024) used a normalizing treatment to promote martensitic phase transformation and eliminate the elemental segregation zone to improve the mechanical properties—such as tensile strength and impact toughness—of U71Mn steel linear friction welded joints. However, surface strengthening technologies such as laser cladding and laser quenching face challenges in large-scale practical applications due to their limitations of high process complexity, harsh operating conditions, and high production costs (Hu et al., 2018; Lei et al., 2018; Zhao JZ et al., 2021; Ding et al., 2022). Therefore, there is high demand for developing new rail welded joint strengthening technologies, which could improve the weak links in railway lines. At the same time, most relevant existing research has focused on the strengthening of single welded joints, while comparative studies of joints prepared by different welding methods are scarce.

Laminar plasma quenching (LPQ) is an advanced surface treatment technology. It employs gas discharge to generate high-energy plasma flow, which heats metal surfaces to temperatures exceeding the solid-state phase transition threshold. Subsequently, a hardened layer composed of ultrafine martensite forms on the metal surface through rapid cooling (Xu et al., 2020, 2021). This treatment enhances the surface hardness of the rail without altering its internal microstructure and properties, significantly improving its resistance to RCF and wear (Bai et al., 2024; Wang K et al., 2024a; Zhu et al., 2024). LPQ has several advantages, including high efficiency, minimal thermal distortion, process flexibility, and low cost, making it promising for applications in various fields, such as the railway industry, mechanical additive manufacturing, aerospace, metallurgy, and renewable energy (Kenel et al., 2017; Guo et al., 2021; Wang CS et al., 2024).

Given the exceptional performance of LPQ technology in enhancing material surface strength, its application to rail welded joints is expected to improve their wear and fatigue resistance, thereby extending their fatigue life. Currently, rail welding primarily employs aluminum thermal welding and flash-butt welding processes (Ilić et al., 1999). In this study, we first analyze the hardness, microstructure, and fatigue damage of two types of welded joints: TWJs and FWJs. Thereafter, roller specimens are prepared from different zones of the joint and subjected to LPQ treatment. The impact of LPQ on the wear resistance and fatigue resistance of the two types of welded joints is then explored through a double-disc test. Additionally, by analyzing the elemental distribution and crystal structure of the quenching zone, we elucidate the differences in wear mechanisms and damage between quenched thermite welded joints (QTJs) and quenched flash-butt welded joints (QFJs). The workflow of our study is illustrated in Fig. S1 of the electronic supplementary materials (ESM). For the reader's convenience, we have provided a list of the abbreviations used in this paper in Table 1.

Table 1 Abbreviations commonly used in this article

Complete expression	Abbreviation
Thermite welded joint	TWJ
Flash-butt welded joint	FWJ
Quenched thermite welded joint	QTJ
Quenched flash-butt welded joint	QFJ
Weld bead	WB
Heat affected	HA
Base material	BM
Weld bead zone of TWJ	TWB
Weld bead zone of FWJ	FWB
Heat affected zone of TWJ	THA
Heat affected zone of FWJ	FHA
Base material zone of TWJ	TBM
Base material zone of FWJ	FBM
Surface-originated fatigue crack	SOFC
Subsurface defect-initiated crack	SDIC
High-angle grain boundary	HAGB
Low-angle grain boundary	LAGB

An analysis of the two types of standard rail welded joints is also offered in the ESM.

2 Double-disc experiment

2.1 Material preparation and experimental procedure

The wheel–rail specimens utilized in the double-disc experiments were sourced from CL60 wheels and two types of welded joints. In order to reduce the influence of the work hardening effect caused by wheel–rail rolling–sliding contact, eight specimens were horizontally cut from two types of welded joints, each at a distance of 10 mm from the rail top. Two specimens were taken from each of the weld bead (WB) zone and the HA zone of two types of joints, while the other four were obtained from the base material (BM) zone; these were used for quenching treatment and control testing, respectively. The welded joint specimens containing WB and HA zones are designated WHA. All specimens were machined into the shape shown in Fig. 1b. Subsequently, the rail welded joint specimens were subjected to LPQ treatment using a four-axis linked computer numerical control (CNC) machine quenching device. The experimental setup is depicted in Fig. 1c.

Previous studies on the process parameters of LPQ have shown that the argon-to-nitrogen ratio, arc current, scanning velocity, and anode nozzle diameter all significantly influence the microstructure and hardness distribution of the hardened layer (Guo et al., 2020; Wang et al., 2022). As the arc current and the scanning velocity increase, both the width and depth of the hardened layer also increase. Additionally, using a 3 mm anode nozzle diameter produces a deeper and narrower hardened layer compared to a 7 mm nozzle (Guo et al., 2020). Furthermore, the depth of the hardened layer gradually decreases with an increasing argon-to-nitrogen ratio and with a greater LPQ nozzle

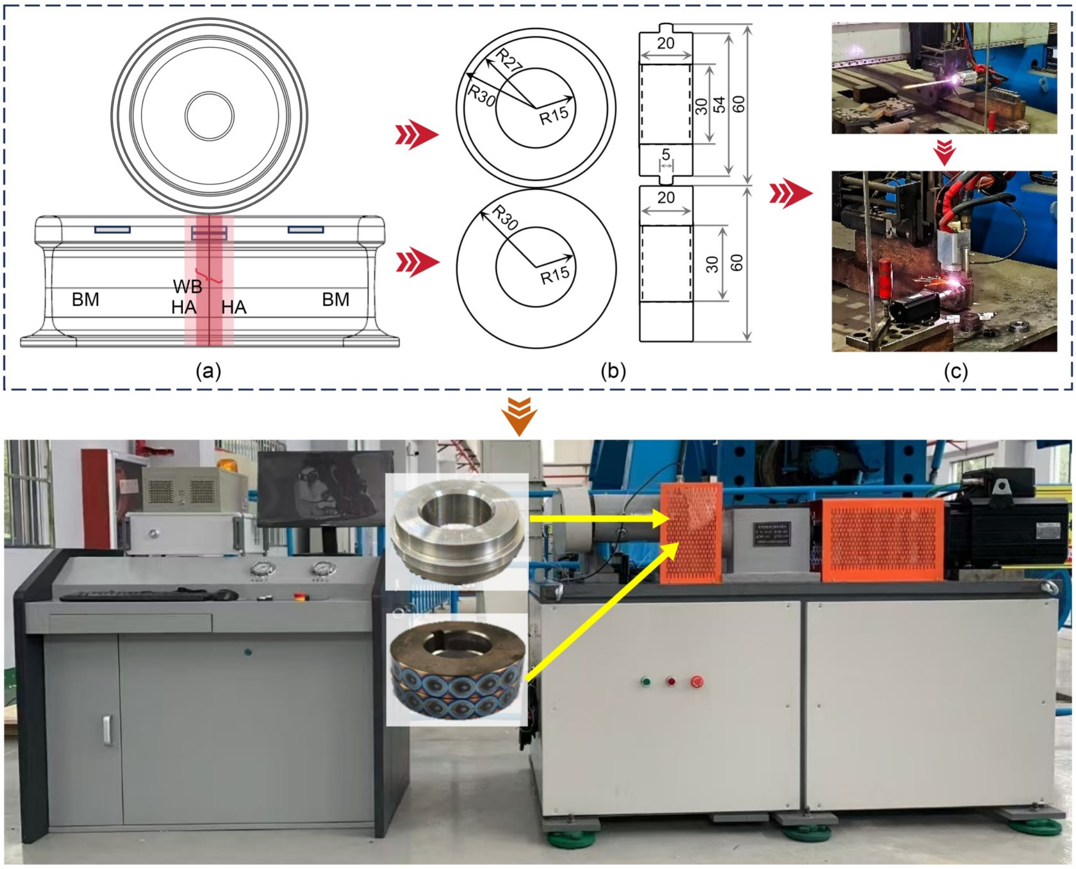

Fig. 1 Schematic diagram of the wheel rail specimens and double-disc tests: (a and b) wheel and rail specimens (unit: mm); (c) experimental setup for LPQ; (d) schematic diagram of the double-disc test

distance (Wang et al., 2022). To achieve a quenching zone with a diameter of 6 mm and a depth of 0.61 mm (Zhu et al., 2024, 2025), the quenching device current was set to 150 A, the scanning speed to 600 mm/min, and the nozzle diameter to 3 mm. The experiment employed a nitrogen-argon mixture with a composition of 40% argon and 60% nitrogen.

A simulation test bench for the wheel–rail contact characteristics (LGPJ-30C, Jinan Xiyan Zhichuang Testing Machine Co., Ltd., China) was utilized to conduct the double-disc experiments in a dry environment, with the specific experimental setup illustrated in Fig. 1d. It is important to note that the contact between the wheel and the welded joint specimen is characterized as a band contact with a length of 5 mm, as depicted in Fig. 1b. In normal train operation, the contact between the wheels and rails typically manifests as single-point or two-point contact. The use of band contact in this experiment is justified by previous experiments, where the rollers with point contact gradually wore down during testing, ultimately resulting in band contact (Zhang et al., 2022). This wear process caused the normal force applied between the wheel and rail specimens to be less than the actual wheel–rail contact force, thereby affecting the accuracy and reliability of the experimental data. The Hertzian contact criterion was applied in this experiment to ensure that the maximum Hertzian contact stress between the wheel–rail specimens was consistent with actual field conditions (Zhang et al., 2022). When the contact stresses are consistent and the mechanical properties of the materials are comparable, we can accurately analyze the mechanical behavior of the wheel–rail material and the fatigue damage under the specified working conditions. For these reasons, a normal force of 5280 N was applied between the wheel and the welded joint specimen to simulate the wheel–rail contact stress under a 25-t axle load condition. During the experiment, the rotational speeds of the wheel and the welded joint specimen were set to 400 and 398 r/min, respectively, and the slip rate was set to 1% (Pereira et al., 2024). Meanwhile, to analyze the changing wear trends of wheel and welded joint specimens, the test cycle times were set to 20000, 40000, 60000, and 80000 revolutions (Shi et al., 2019). Throughout the experiment, a high-pressure air nozzle was employed to blow out the abrasive material and cool the specimens. The characterization and analysis methods utilized following the tests are detailed in Table S3 of the ESM.

2.2 Experimental results

2.2.1 Hardness

Fig. 2 illustrates the hardness of the cross-sections of the QTJ and QFJ specimens. The measurement spacing for the quenching zone is 0.1 mm, while that for the substrate is 0.5 mm. An analysis of the data reveals that the hardness of both the TWJ and FWJ

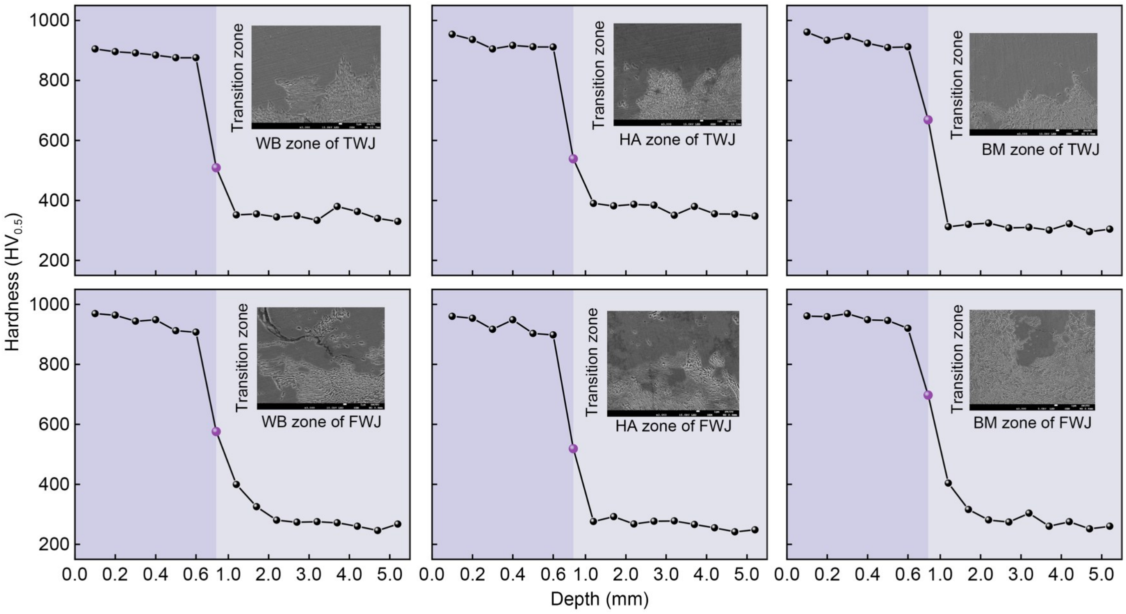

Fig. 2 Cross-sectional hardnesses of the QTJ and QFJ specimens

specimens significantly increases following the LPQ treatment. Specifically, for the QTJ specimens, the microhardness of the matrix structure ranges from 250 to 400 $HV_{0.5}$, whereas the microhardness of the quenching zone reaches as high as 900 to 970 $HV_{0.5}$. In the case of the QFJ specimens, the microhardness of the substrate falls within 300 to 400 $HV_{0.5}$, and the quenching zone achieves a microhardness of 870 to 970 $HV_{0.5}$. Notably, the hardness in the quenching zone of both specimens is highly uniform. Furthermore, the microhardness at the junction of the quenching zone and the substrate remains greater than that of the substrate but less than that of the quenching zone. Additionally, a discernible pattern emerges in the hardness across different zones of the specimens: the hardness in the BM zone exceeds the hardness in the WB zone, and the hardness in the WB zone is greater than that in the HA zone.

2.2.2 Wear mass

Fig. 3 illustrates the wear mass of the wheel–rail specimens before and after quenching. Overall, the wear mass of the wheel–rail specimens before and after quenching increases with the number of cyclic

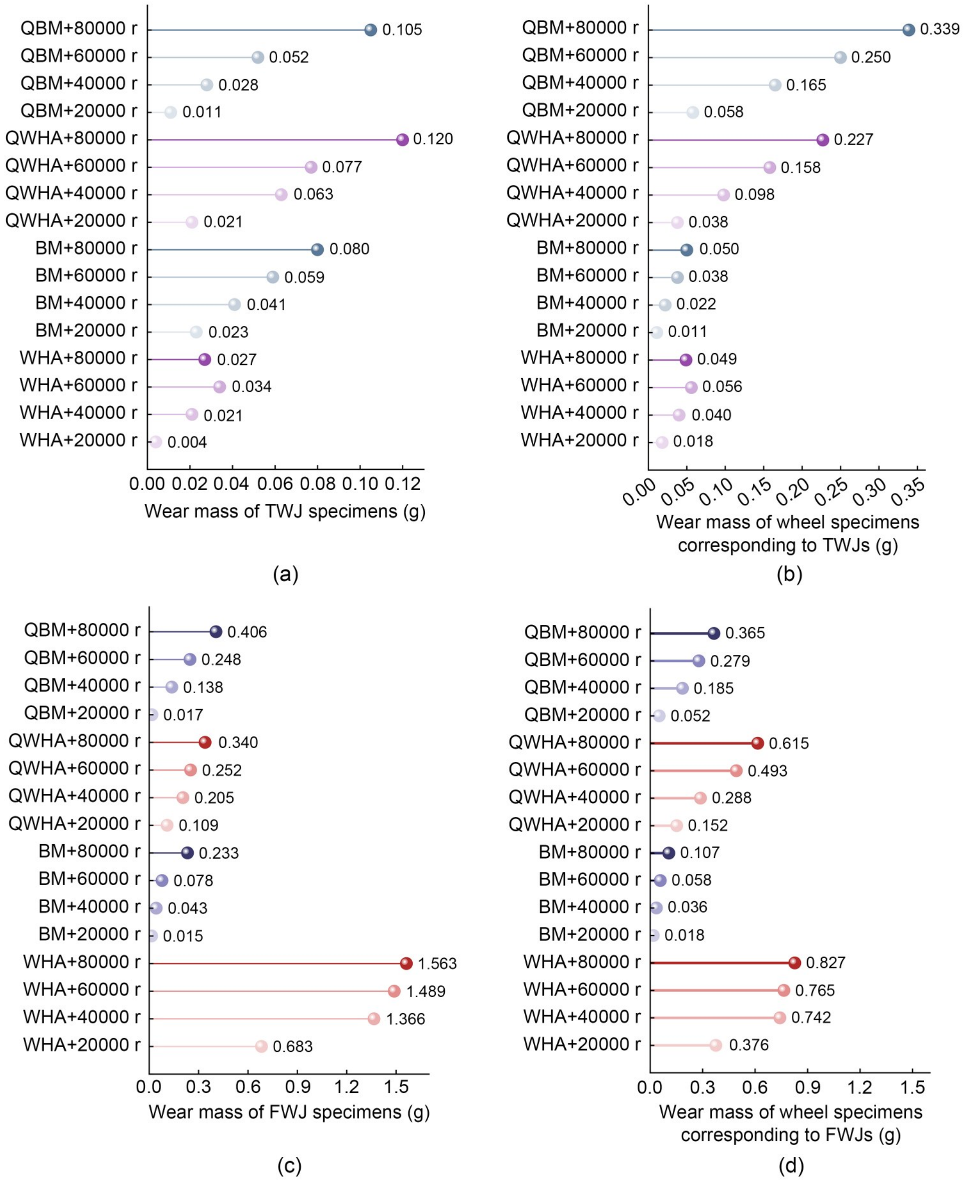

Fig. 3 Wear mass of joint (a and c) and wheel (b and d) specimens before and after LPQ treatment: (a and b) TWJs; (c and d) FWJs. QWHA: quenched WHA specimen; QBM: quenched BM specimen

loads, given a constant applied normal force. For TWJs, the wear of the quenched WHA specimens was more severe than that of the unquenched specimens. This is attributed to the high-temperature filling process of thermit welding, which utilizes molten metal that cools at a slower rate, leading to the formation of coarse grains, porosity, inclusions, and compositional segregation (Liu et al., 2021). Pores and inclusions act as points of stress concentration, and the quenching process promotes the expansion of microcracks along these defects, ultimately resulting in spalling. Additionally, the increase in hardness of the rail specimens, which surpasses that of the wheel specimens, results in more severe wear of wheel specimens corresponding to the QTJ specimens. In contrast, for FWJs, the quenching treatment enhances the wear resistance of the WHA specimens. The wear mass at 20000, 40000, 60000, and 80000 cycles was reduced by 84%, 85%, 83%, and 78%, respectively. This improvement is due to the finely equiaxed grain structure of the original FWJ, which is further refined by the quenching treatment, significantly enhancing the specimens' hardness and resistance to plastic deformation. For TWJs, the wear mass of the BM specimens after quenching was greater than that of the WHA specimens, while the opposite was observed for FWJs. The minimal difference in wear mass between the WHA and BM specimens for both types of welded joints after quenching suggests that the LPQ process effectively balances abrasion across different zones of the welded joints, mitigates irregularities in the welded joints of the rails, and reduces the wheel–rail impact at the joints.

2.2.3 Fatigue damage analysis

The surface injuries observed in various zones of the QTJ specimens are illustrated in Fig. 4. These injuries are primarily characterized by significant spalling and material accumulation within the quenching zone, with no evident fatigue cracks or secondary cracks detected. Furthermore, a distinct boundary can be observed between the quenching zone and the BM, which is attributed to the difference in hardness between the

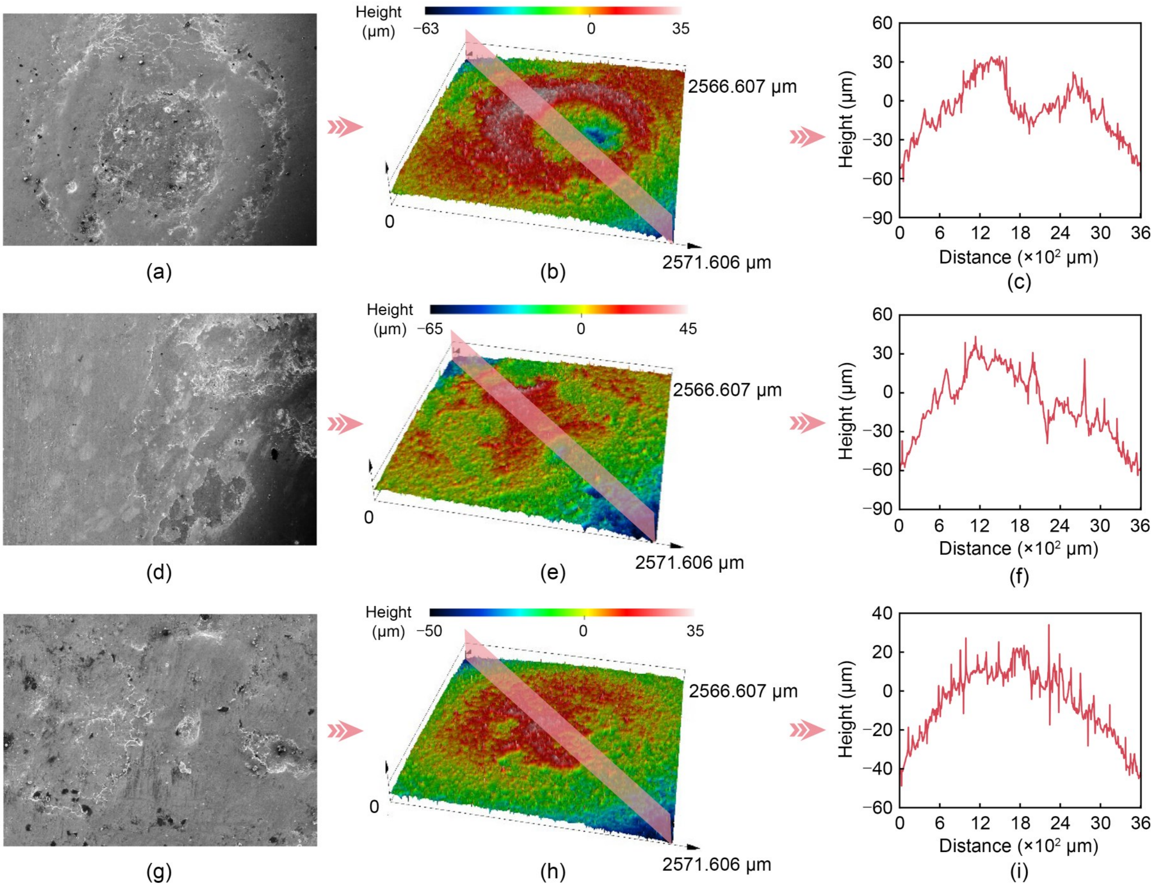

Fig. 4 Morphological analysis of surface damage on the QTJ specimens: (a–c) WB; (d–f) HA; (g–i) BM

two zones and leads to the discrepancy in wear. During prolonged rolling contact between the wheel and rail, this wear differential will gradually accumulate, ultimately resulting in a height difference that highlights the boundary between the hardened zone and the BM (Bai et al., 2024). To further analyze the morphological characteristics of each zone of the QTJ specimen, contour lines were extracted at the same section from 3D images obtained using a laser confocal microscope, as illustrated in Figs. 4c, 4f, and 4i. The heights of the structural buildup in the WB zone, HA zone, and BM zone are measured at 34.3, 43.4, and 34.1 μm, respectively. Additionally, significant spalling pits are evident in the quenching zone of the specimens. The center of the quenching zone exhibits unevenness, which is attributed to localized ablation and results in increased roughness in that area (Wang et al., 2023b).

The surface injuries of the QFJ specimens in each zone are illustrated in Fig. 5. In the BM zone, surface damage is primarily characterized by the presence of primary cracks, secondary cracks, and significant spalling phenomena at the edge of the quenching zone, as depicted in Figs. 5c and 5f. In contrast, the surface cracks in the WB and HA zones are more densely distributed, as shown in Figs. 5a and 5b, with the crack propagation path being nearly perpendicular to the rolling direction. Compared to those in the WB and BM zones, the surface cracks in the HA zone are longer, more numerous, and exhibit greater relative density. Cracks in the HA zone initiate at the center of the quenching zone and extend toward its edge. Notably, both the WB and BM zones display structural material buildup at the edge of the quenching zone in the form of flaky skinning, despite having a lower number of cracks. Moreover, the fatigue cracks in the WB and BM zones propagate rapidly outward after initiation, leading to significant spalling.

Fig. 6 presents OM and SEM images depicting the cross-sectional damage in various zones of the QTJ specimens. The fatigue damage observed in the specimens is primarily characterized by subsurface defect-initiated crack (SDIC), accompanied by slight spalling. The most severe damage was identified in the HA zone, which exhibited multiple minor cracks (<100 μm), followed by the WB zone, while the BM zone displayed the least severe damage. This pattern of damage corresponds to the microstructural conditions discussed in Section S1 of the ESM. The thermit welding process introduces defects such as porosity, inclusions, and under-welding in both the WB zone and the HA zone, as illustrated in Figs. 6a and 6c. These defects serve as initiation points for cracks during the experiments

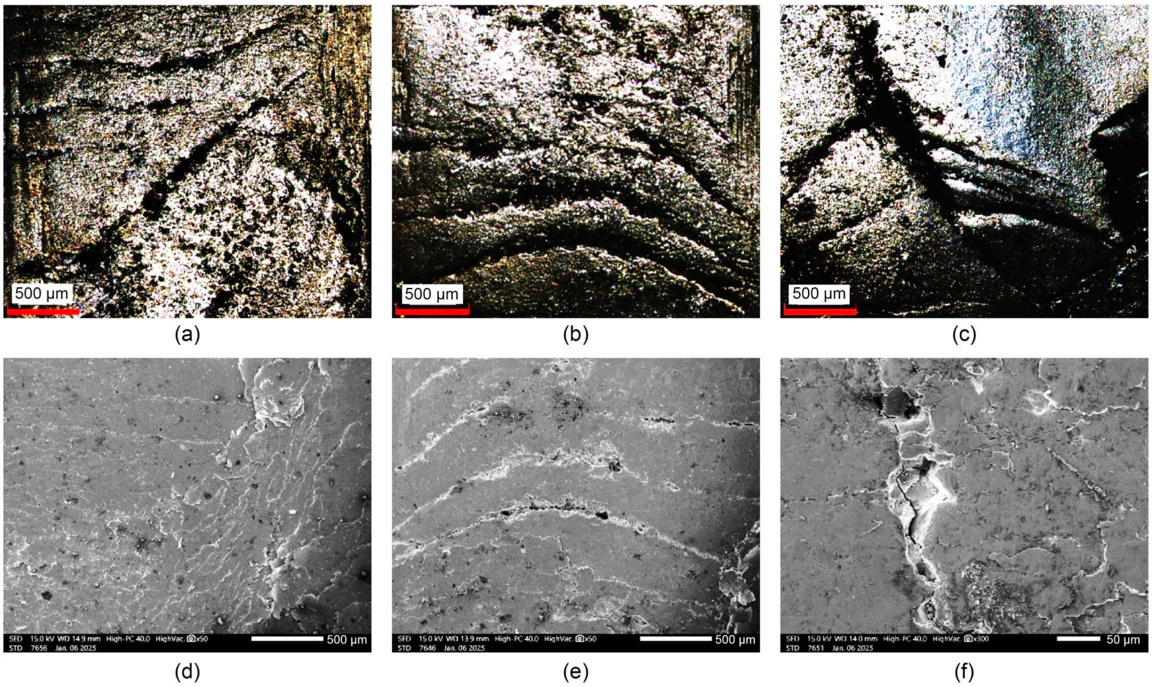

(a) (b) (c)

(d) (e) (f)

Fig. 5 Optical microscope (OM) (a–c) and scanning electron microscope (SEM) (d–f) images of surface damage on QFJ specimens: (a and d) WB; (b and e) HA; (c and f) BM

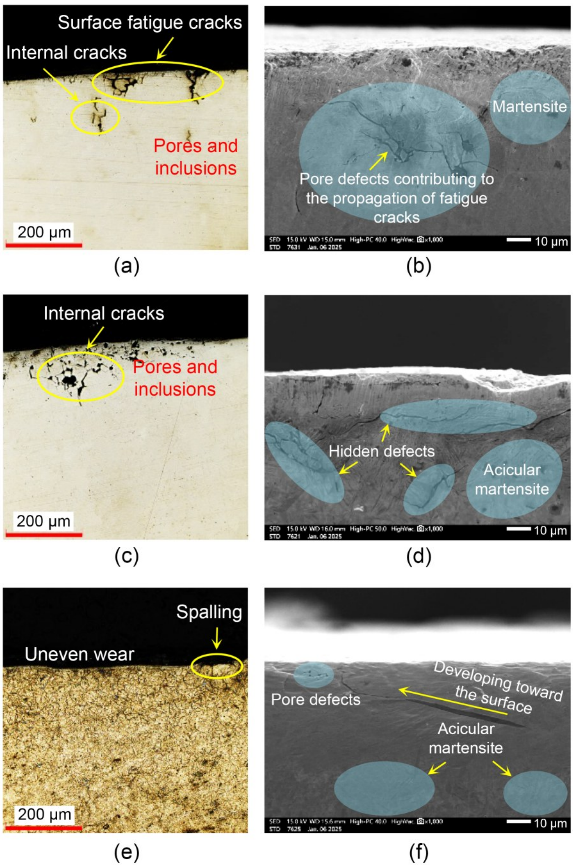

Fig. 6 OM (a, c, and e) and SEM (b, d, and f) images of cross-sectional damage in QTJ specimens: (a and b) WB; (c and d) HA; (e and f) BM

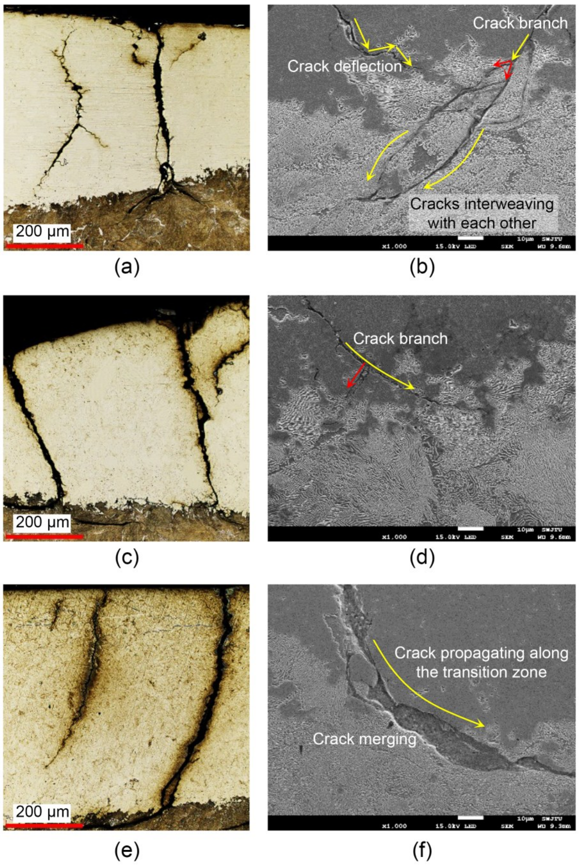

Fig. 7 OM (a, c, and e) and SEM (b, d, and f) images of cross-sectional damage in QFJ specimens: (a and b) WB; (c and d) HA; (e and f) BM

on the quenching specimens and gradually evolve into concealed injuries. Furthermore, these cracks are predominantly concentrated within 70 μm of the specimen surface and do not compromise the substrate. With prolonged loading, the cracks progressively extend toward the surface of the specimen, partially leading to spalling.

OM and SEM images of the profile damage in various zones of the 1QFJ specimens after testing are shown in Fig. 7. Surface-originated fatigue cracks (SOFCs) are observed in all zones of the specimen, and the material exhibits severe internal fragmentation. Some SOFCs extend toward the surface following deflection, while wear causes the material above the cracks to continuously thin. Eventually, these cracks connect with the surface, leading to large-scale spalling of the material. Additionally, some SOFCs expand to the transition zone at large angles, forming branching cracks. Cracks with this type of extension typically do not lead to large-scale spalling of the material above them. SDICs (Fig. 7a) are observed in the HA zone. In the transition zone, some branching cracks develop for a period of time and subsequently intersect. When these cracks merge, the intermediate material is sheared and detached from the substrate, becoming a fragmented material of the intermediate layer. The cracks then coalesce into a longer crack, as illustrated in Figs. 7b and 7f. This phenomenon is referred to as crack interweaving. Furthermore, it is noteworthy that when the fatigue crack reaches the transition zone, it does not continue to propagate into the BM. This behavior is attributed to the significant hardness gradient between the quenching zone and the BM (Fig. 2). Additionally, the interior of the quenching zone primarily consists of plate-like martensite, which has poor toughness, whereas the substrate is predominantly composed of pearlite, an exceptionally tough material (Bai et al., 2024). The disparity in toughness between the quenching zone and the substrate interface leads to pronounced boundary effects, which inhibit crack propagation into the substrate and can help mitigate potential safety hazards for railway operations.

Untreated welded joint specimens are primarily composed of pearlite and ferrite. Under cyclic loading, when the yield stress on the surface of the wheel–rail material exceeds its stability limit, ratcheting failure may be induced. In the initial stage, plastic deformation accumulates on the material's surface, causing microcracks to form. As the number of rolling contacts increases, these cracks propagate toward the surface, resulting in small-scale peeling; this ultimately develops into larger areas of spalling. With the continued action of contact stress, some cracks propagate inward into the rail material (>4800 μm), posing a serious threat to the structural safety of the railway, as illustrated in Fig. S7 of the ESM. Following LPQ treatment, the fatigue cracks become confined to the quenching and transition zones (<610 μm), indicating that LPQ treatment effectively suppresses crack development.

Based on the cross-sectional damage analysis presented in Figs. 6 and 7, the quenching welded joint specimens exhibit two mechanisms of crack initiation under cyclic loading: SOFC and SDIC. Crack propagation can be categorized into three typical modes: branching propagation, crack interweaving, and deflection trajectory. The experimental results of this paper indicate that crack initiation in QTJ specimens is predominantly governed by the SDIC mechanism, with the propagation exhibiting notable path deflection characteristics along with localized crack branching phenomena. In contrast, QFJ specimens display both SOFC and SDIC mechanisms, and their crack propagation exhibits multi-mode coupling characteristics, including branching propagation, crack interweaving, and deflection trajectory (B-C-D). Section 3 will explore the reasons for the differences in the crack propagation mechanisms of the QTJ and QFJ specimens.

3 Discussion

3.1 Element distribution and wear mechanism

Energy-dispersive X-ray spectroscopy (EDS) line scanning was used to measure the elemental distributions in the TWB, THA, FWB, FHA, and BM zones after 80000 cycles. The EDS lines were perpendicular to and parallel to the transition zone, as illustrated in Figs. 8a and 9a, respectively. By analyzing the elemental distributions, the wear mechanisms of QTJs and QFJs can be elucidated.

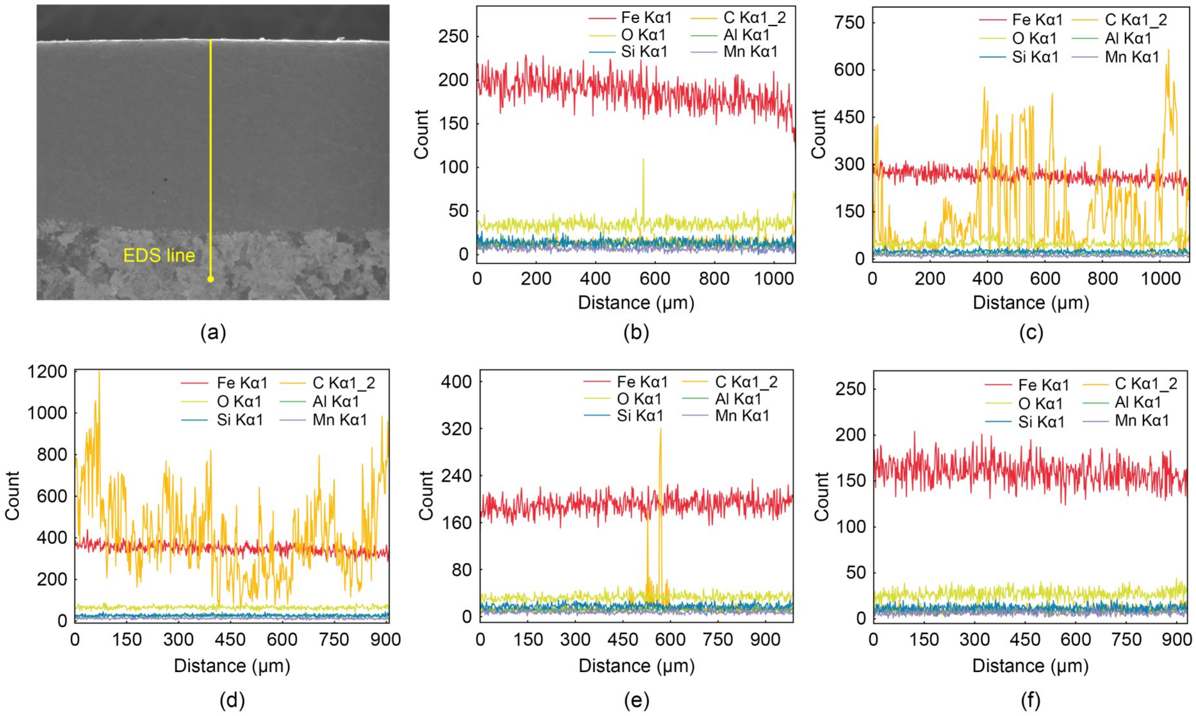

(a) (b) (c)

(d) (e) (f)

Fig. 8 EDS line scans of two types of quenched welded joints perpendicular to the transition zone: (a) EDS line scan of the physical image; (b) TWB; (c) THA; (d) FWB; (e) FHA; (f) BM

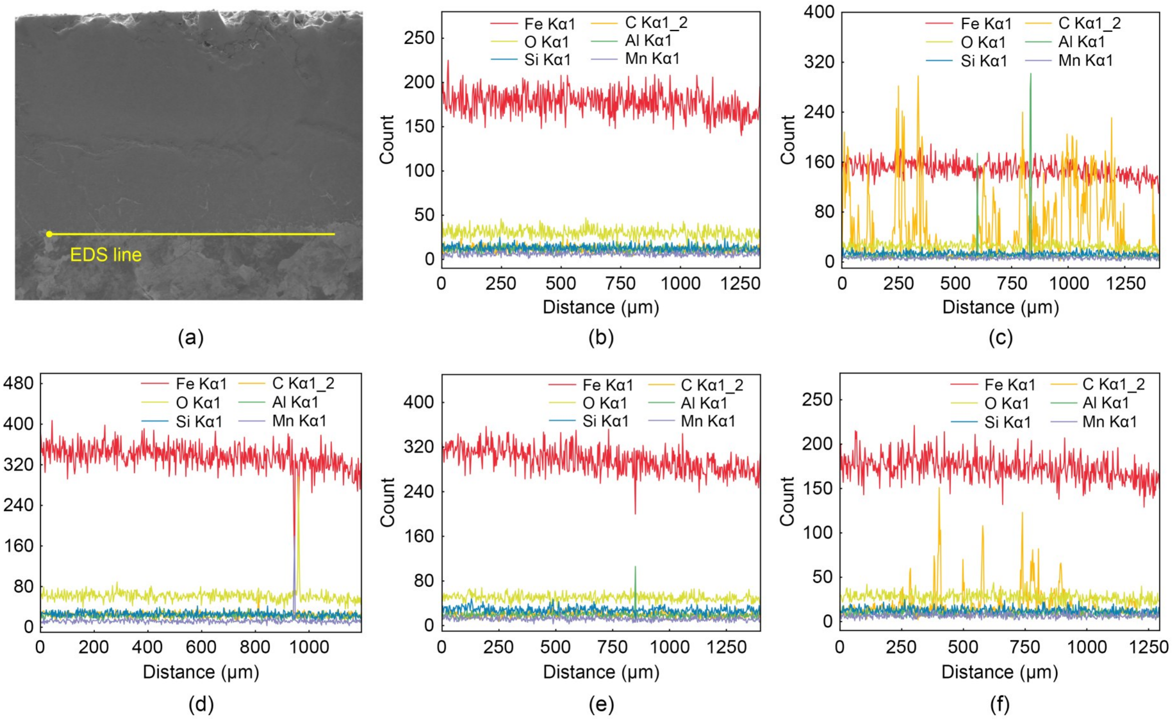

(a) (b) (c)
(d) (e) (f)

Fig. 9 EDS line scans of two types of quenched welded joints aligned with the transition zone: (a) EDS line scan of the physical image; (b) TWB; (c) THA; (d) FWB; (e) FHA; (f) BM

Comparing the line scans of the two types of welded joints in Fig. 8, it is evident that the concentration of iron (Fe) elements in the TWB zone, THA zone, FWB zone, and BM zone has decreased to a certain extent, with the exception of the FHA zone. This reduction is attributed to cyclic friction, which raises the surface temperature of the specimen, causing the martensitic surface in the quenching zone to oxidize and form Fe_2O_3/Fe_3O_4. After the oxide layer peels off, oxidation reactions persist, resulting in a continuous decrease in the Fe content (Shen et al., 2024). Concurrently, the cementite in the quenching zone becomes elongated and fibrotic due to plastic deformation on the specimen's surface, ultimately increasing the surface carbon (C) content. This notable rise in surface C content contributes to an increase in surface hardness, which is a phenomenon known as work hardening (Li et al., 2021). Additionally, the carbides (Fe_3C) formed during quenching were fragmented and redistributed under cyclic shear stress throughout the experiment, resulting in fluctuations in the distribution of C elements within the quenching zone, as illustrated in Figs. 8c–8e. Unlike in the WB and HA zones, there is no significant change in the elements of the BM zone. This is because the BM develops a small and uniform lath martensite microstructure after quenching, which exhibits high hardness and toughness (Zhao et al., 2018). The uniform distribution of carbides in the substrate leads to minimal fragmentation under cyclic loading conditions. Furthermore, there is no interference from aluminum (Al) inclusions in the substrate, and the manganese (Mn) is uniformly held in solid solution.

Following quenching treatment, the phase composition of the quenching zones in the rail welded joints transforms rapidly, resulting in the formation of a soft-hard interface with the substrate. The hardness gradient at the boundary between the quenching zone and the substrate is steep, as illustrated in Fig. 2. Therefore, it is particularly important to analyze the characteristics of the elemental distribution in the transition zone between the quenching zone and the substrate. By comparing the line scans of the two types of joints in Fig. 9, it can be observed that the content of Fe in all zones exhibits a decreasing trend along the EDS scanning trajectory. Nonsteady-state fluctuations of the C elements were detected in the THA and BM zones, which are associated with the solid solution and precipitation of carbides during the quenching process (Wang K et al., 2024a). Discrete peaks of aluminum (Al) enrichment were observed in the HA zones of both samples, with QTJs displaying bimodal characteristics and QFJs showing a unimodal structure. The presence of Al in the THA and FHA zones may be attributed to Al_2O_3 inclusions that result from aluminum thermal reactions and environmental pollutants, respectively. Additionally, a manganese−oxygen (Mn–O)-coupled enrichment region was identified in the FWB zone, indicating a significant spatial correlation between these two elements.

In Section 2.2.3, we demonstrated that crack interweaving is an important process in crack propagation, typically occurring in the transition zone of QFJ specimens. To further analyze the impact of the element distribution in the transition zone on crack propagation, EDS surface scans were performed. Specifically, Fig. 10a shows an electron micrograph, Fig. 10b shows an EDS layered image, and Figs. 10c–10f are distribution maps of Fe, O, C, and Al elements, respectively. In these maps, brighter colors indicate a higher concentration of elements, while darker colors indicate a lower concentration. One can see that there is significant enrichment of oxygen within the crack, and the ferrite in the pearlite structure undergoes a series of chemical reactions with this oxygen, resulting in the deposition of Fe_2O_3 inclusions inside the crack. Under the action of cyclic loading, these inclusions may induce stress concentration within the crack, thereby exacerbating crack propagation. Previous studies on the deposition of carbides in the subsurface of steel rails have shown that such deposition can negatively affect the material's uniformity and resistance to plastic deformation (Wang K et al., 2024b). Furthermore, the difference in electrochemical potential between carbides and ferrites in the steel rail can lead to localized galvanic corrosion, accelerating crack propagation (Wang K et al., 2024b). Consequently, we investigated the distribution of elemental carbon (C) within the cracks of the transition zone, as illustrated in Fig. 10e. The low content of carbon within the crack suggests that its role in accelerating crack propagation is minimal. The low carbon content may be attributed to the diffusion and redistribution of carbon elements caused by the plastic deformation of the rail's subsurface under cyclic loading.

3.2 Crystal structure and damage difference

Fig. 11 presents an inverse pole figure (IPF) of the TWJs and FWJs following LPQ treatment. The black and white lines in the figure denote high-angle grain boundaries (HAGBs, >15°) and low-angle grain boundaries (LAGBs, 2°–15°), respectively. The figure reveals that the grain size in the quenching zone is relatively

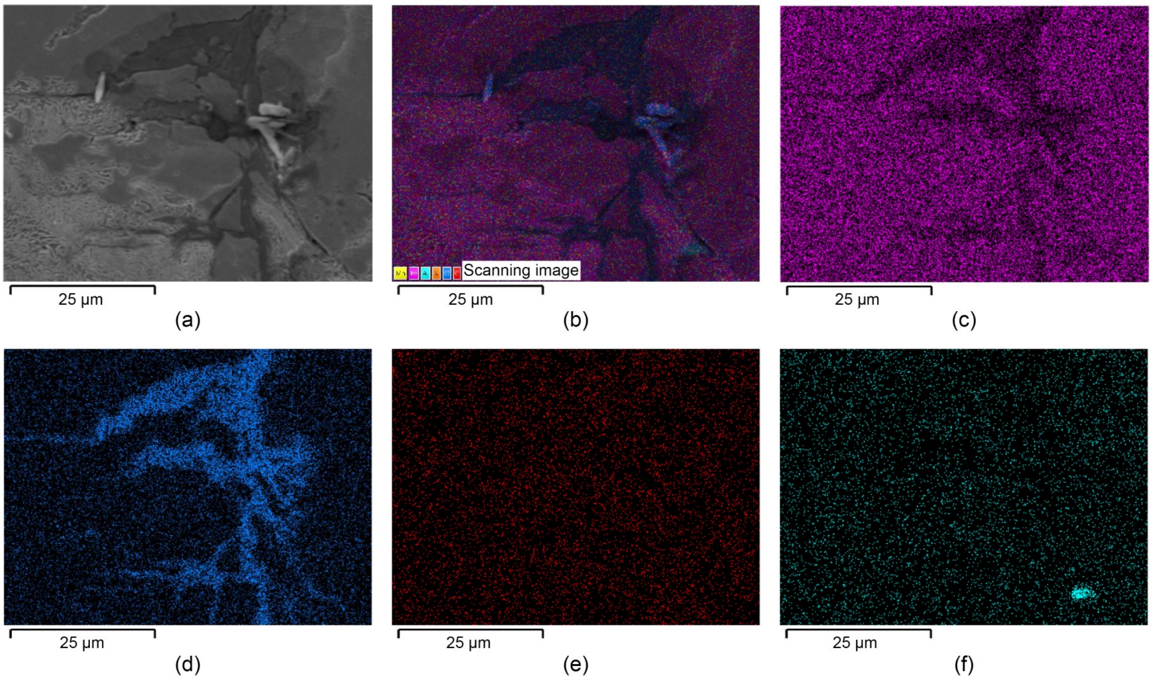

Fig. 10 EDS surface scans of cracks in the transition zone of the QFJ specimen: (a) scanning electronic image; (b) EDS layered image; (c–f) distribution diagrams of Fe (c), O (d), C (e), and Al (f)

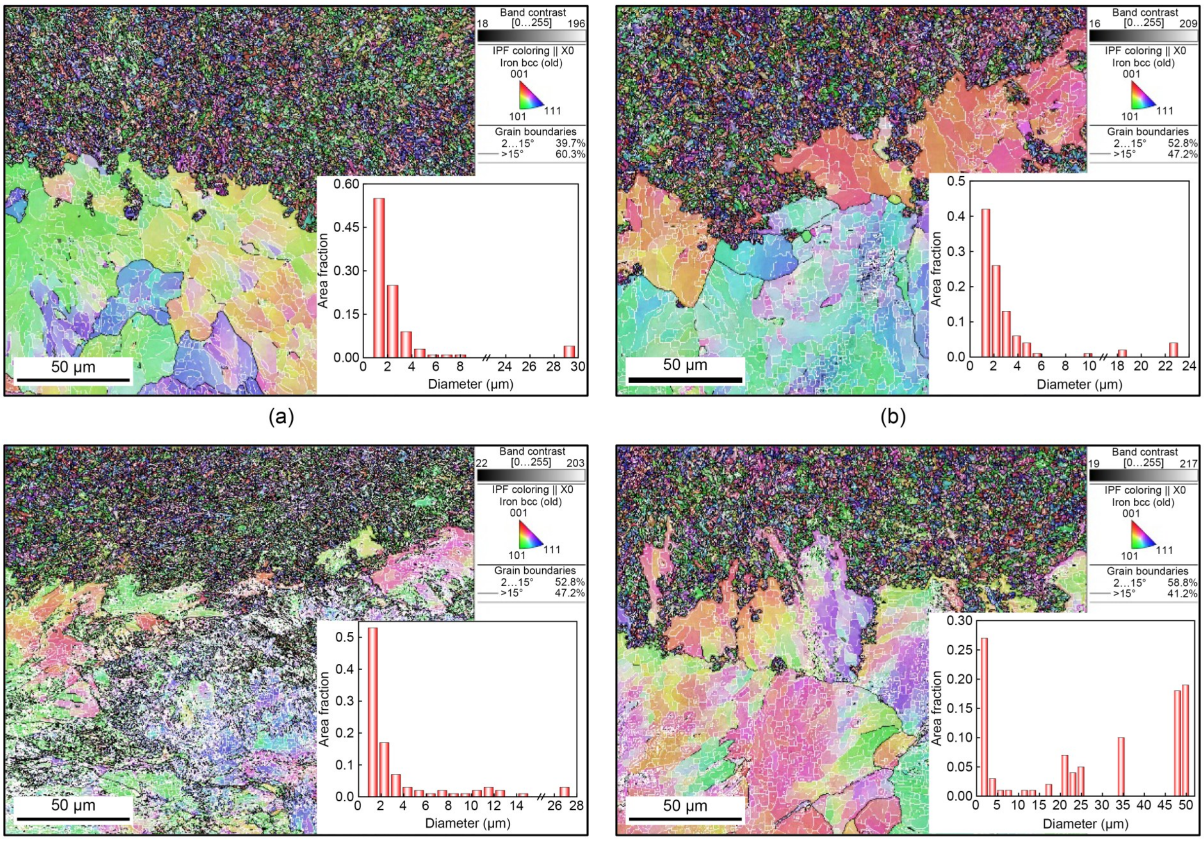

(a)

(b)

(c)

(d)

Fig. 11 IPF maps of QTJs and QFJs in different zones: (a) TWB; (b) THA; (c) FWB; (d) FHA

small compared to that in the substrate. The average grain sizes in the quenching zone for the four regions (TWB, THA, FWB, and FHA) are (1.93±0.57) μm, (1.63±0.46) μm, (2.04±0.60) μm, and (1.90±0.53) μm, respectively, indicating a high degree of uniformity. Furthermore, the quenching zone exhibits a higher density of HAGBs compared to the substrate. The increase in HAGBs is often associated with grain refinement, as the formation and increasing presence of HAGBs are typically linked to recrystallization, a process that can lead to grain refinement. Previous studies on grain refinement and fatigue performance have demonstrated that grain refinement reduces stress concentration and promotes deformation uniformity by increasing the grain boundary area, thereby inhibiting the initiation of fatigue cracks at the grain boundaries (Zhao P et al., 2021). Additionally, the intricate and complex morphology of grain boundaries can effectively impede crack propagation, ultimately leading to a significant improvement in the fatigue performance of the material (Zhao P et al., 2021). The above statement explains the conclusion in Section 2.2.3 regarding LPQ suppressing crack propagation.

Fig. 11 illustrates that the proportions of HAGBs in the TWB, THA, FWB, and FHA zones are 39.7%, 52.8%, 52.8%, and 58.8%, respectively, which presents an overall distribution law of "HA>WB" and "QFJs> QTJs". The atomic arrangement at HAGBs is relatively disordered with many lattice defects, which makes the chemical bonds at the grain boundaries weak and prone to stress concentration. Furthermore, atomic diffusion and slip easily occur at HAGBs, leading to a reduction in the toughness of the material. Consequently, when subjected to external forces, cracks are more likely to propagate along HAGBs. This explains why the HA zone of the same joint experiences more severe damage compared to the WB zone after quenching treatment, while the damage in the QFJs (with a crack length of approximately (520±40) μm) is more serious than that in the QTJs (crack length of (50±20) μm).

According to previous research, the dislocation motion induced by cyclic loading is the primary driving force behind fatigue failure (Gallo et al., 2022; Sallaba et al., 2022). Under alternating stress, dislocations accumulate at grain boundaries and second-phase particles, forming localized stress concentrations; this promotes the formation of slip bands and may directly induce microcracks. With the continuous action of cyclic loads, the slip bands continue to widen and deepen, interacting with one another and deteriorating the material's internal microstructure (Maich et al., 2024). When dislocation motion and slip bands develop to a certain extent, stress-induced atomic migration and redistribution within the material result in the formation of vacancy defects. These atomic-scale vacancies evolve into microcracks through aggregation and merging. Initially, microcracks grow within the same grain but later propagate across grain boundaries toward adjacent grains, ultimately leading to macroscopic fatigue damage.

The extent of material damage can be characterized by the dislocation density (Wang et al., 2023a). Based on the work of Tan et al. (2024), the distribution of kernel average misorientation (KAM) can serve as a quantitative indicator of geometrically necessary dislocation (GND) density. Thus, the KAM value is positively correlated with material fatigue damage. The experiments in Section 2 showed that the fatigue damage of QTJs/QFJs is primarily confined to the quenching zone; this aligns with the observations from Fig. 12, where the KAM value in the quenching zone is significantly higher than that of the matrix material. Tabaie et al. (2021) found that reducing welding heat input can suppress the dynamic recrystallization (DRX) process, leading to increased KAM values along the original grain boundaries and within the grains. As a result, QFJs exhibit higher KAM values than QTJs. High-density dislocations can enhance resistance to fatigue crack propagation, providing a theoretical explanation for the observed differences between QFJs and QTJs in terms of quenching-zone damage (Li et al., 2022).

Of course, real outdoor environments are much more complex than laboratories. Our experiments did not consider factors such as the vibration of the wheel–rail system, the nonlinear characteristics of wheel loads, and the variability of weather, which may result in inaccuracies when applying the findings to practical

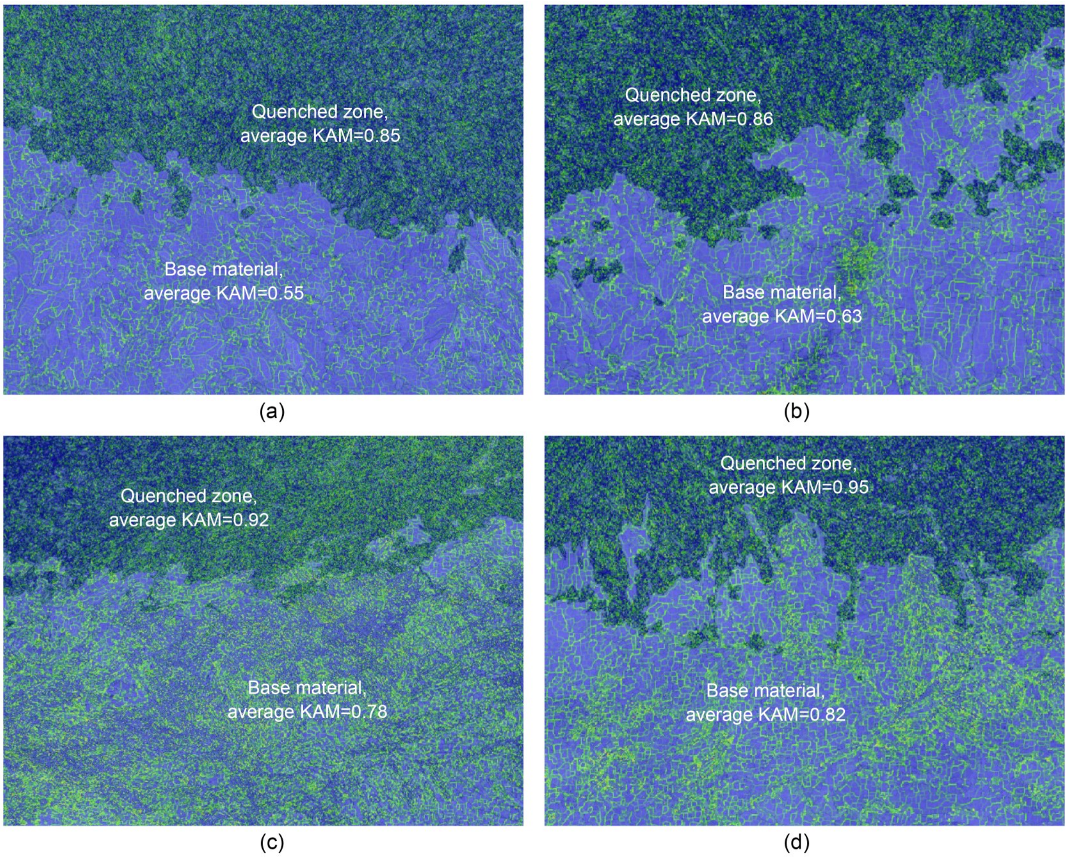

Fig. 12 KAM maps of QTJs and QFJs in different zones: (a) TWB; (b) THA; (c) FWB; (d) FHA

scenarios (Wang et al., 2025). Therefore, further work should be conducted on a full-size test bench or in field tests, considering the coupling effect of environmental and train loads.

4 Conclusions

The fatigue damages of on-site TWJs and FWJs were compared and analyzed. Subsequently, we explored the influence of LPQ on the wear resistance and fatigue resistance of these two types of joints through a dual disc test. Finally, based on analysis of the element distribution and crystal structure in the quenching zone, we elucidated the wear mechanisms and differences in damage between QTJs and QFJs. There are some meaningful observations in this study, which are presented as follows:

1. The LPQ process was revealed to significantly enhance the wear resistance of FWJs, reducing the wear mass by 78%–85%. In contrast, following LPQ treatment, the TWJs exhibited increased wear due to internal defects, such as pores and inclusions.

2. LPQ can also suppress the formation of cracks in welded joints. Crack propagation in the QTJ is governed by the SDIC mechanism, which displays characteristics of deflection trajectory and branching propagation. QFJ is associated with two mechanisms—SOFC and SDIC—and its crack propagation exhibits multi-mode coupling characteristics of B-C-D.

3. Significant oxidative corrosion occurs within the cracks of the transition zone in QFJ. The observed fluctuations in iron (Fe) and oxygen (O) contents are associated with the spalling of the surface oxide layer of the specimen, while the fluctuation of carbon (C) is linked to the solid solution and precipitation of carbides during the quenching process.

4. The difference in the density of HAGBs and dislocations explains why the fatigue damage in the HA zone is more severe than that in the WB zone for the same joint, while the damage in QFJs is greater than that in QTJs.

Acknowledgments

This work is supported by the National Natural Science Foundation of China (Nos. 52388102, 52478474, 52472458, and U23A20666), the Major Program of Sichuan Provincial Natural Science Foundation of China (Nos. 2025NSFTD0013, 2024NSFSC0003, and 2025YFHZ0035).

Author contributions

Jingmang XU and Kai WANG designed the research. Wenfeng GAO and Taoshuo BAI processed the corresponding data. Hui ZHU wrote the first draft of the manuscript. Jian YANG helped to organize the manuscript. Hui ZHU, Yao QIAN, and Ping WANG revised and edited the final version.

Conflict of interest

Jingmang XU, Hui ZHU, Wenfeng GAO, Taoshuo BAI, Jian YANG, Kai WANG, Yao QIAN, and Ping WANG declare that they have no conflict of interest.

References

Bai TS, Xu JM, Zhu H, et al., 2024. Investigation into the wear evolution and fatigue crack propagation behaviour of rails subjected to laminar plasma discrete quenching and tempering treatment. *Wear*, 554-555:205470. https://doi.org/10.1016/j.wear.2024.205470

Ding HH, Mu XP, Zhu Y, et al., 2022. Effect of laser claddings of Fe-based alloy powder with different concentrations of WS_2 on the mechanical and tribological properties of railway wheel. *Wear*, 488-489:204174. https://doi.org/10.1016/j.wear.2021.204174

Fang XY, Zhang HN, Ma DW, et al., 2022. Influence of welding residual stress on subsurface fatigue crack propagation of rail. *Engineering Fracture Mechanics*, 271:108642. https://doi.org/10.1016/j.engfracmech.2022.108642

Gallo P, Lehto P, Malitckii E, et al., 2022. Influence of microstructural deformation mechanisms and shear strain localisations on small fatigue crack growth in ferritic stainless steel. *International Journal of Fatigue*, 163:107024. https://doi.org/10.1016/j.ijfatigue.2022.107024

Ghazanfari M, Tehrani PH, 2021. Increasing fatigue crack initiation life in butt-welded UIC60 rail by optimization of welding process parameters. *International Journal of Fatigue*, 151:106367. https://doi.org/10.1016/j.ijfatigue.2021.106367

Guo D, Yu DP, Zhang P, et al., 2020. Laminar plasma jet surface hardening of the U75V rail steel: insight into the hardening mechanism and control scheme. *Surface and Coatings Technology*, 394:125857. https://doi.org/10.1016/j.surfcoat.2020.125857

Guo D, Yu DP, Zhang P, et al., 2021. Laminar plasma jet surface hardening of P20 mold steel: analysis on the wear and corrosion behaviors. *Surface and Coatings Technology*, 415:127129. https://doi.org/10.1016/j.surfcoat.2021.127129

Hernández FCR, Okonkwo AO, Kadekar V, et al., 2016. Laser cladding: the alternative for field thermite welds life extension. *Materials & Design*, 111:165-173. https://doi.org/10.1016/j.matdes.2016.08.061

Hu ZH, Zhu HH, Zhang CC, et al., 2018. Contact angle evolution during selective laser melting. *Materials & Design*, 139:304-313. https://doi.org/10.1016/j.matdes.2017.11.002

Hultgren G, Mansour R, Barsoum Z, 2023. Fatigue strength assessment of welded joints incorporating the variability in local weld geometry using a probabilistic framework. *International Journal of Fatigue*, 167:107364. https://doi.org/10.1016/j.ijfatigue.2022.107364

Ilić N, Jovanović MT, Todorović M, et al., 1999. Microstructural and mechanical characterization of postweld heat-treated thermite weld in rails. *Materials Characterization*, 43(4):243-250. https://doi.org/10.1016/S1044-5803(99)00006-6

Kenel C, Dawson K, Barras J, et al., 2017. Microstructure and oxide particle stability in a novel ODS γ-TiAl alloy processed by spark plasma sintering and laser additive manufacturing. *Intermetallics*, 90:63-73. https://doi.org/10.1016/j.intermet.2017.07.004

Lei JB, Shi C, Zhou SF, et al., 2018. Enhanced corrosion and wear resistance properties of carbon fiber reinforced Ni-based composite coating by laser cladding. *Surface and Coatings Technology*, 334:274-285. https://doi.org/10.1016/j.surfcoat.2017.11.051

Li SR, Wang XM, Dong WJ, et al., 2025. Peridynamic analysis of rolling contact fatigue crack propagation in rail welding joints with pore defects. *International Journal of Fatigue*, 190:108612. https://doi.org/10.1016/j.ijfatigue.2024.108612

Li W, Chang KR, Zeng PY, et al., 2021. Impact wear of flash- and aluminothermic-welded hypereutectoid steel rail joints. *Tribology Transactions*, 64(4):644-657. https://doi.org/10.1080/10402004.2021.1893874

Li XY, Ma R, Liu X, et al., 2022. Effect of laser shock peening on fatigue properties of U75VG rail flash-butt welding joints. *Optics & Laser Technology*, 149:107889. https://doi.org/10.1016/j.optlastec.2022.107889

Liu P, Sun SY, Hu JY, 2019. Effect of laser shock peening on the microstructure and corrosion resistance in the surface of weld nugget zone and heat-affected zone of FSW joints of 7050 Al alloy. *Optics & Laser Technology*, 112: 1-7. https://doi.org/10.1016/j.optlastec.2018.10.054

Liu Y, Tsang KS, Zhi'En ET, et al., 2021. Investigation on material characteristics and fatigue crack behavior of thermite welded rail joint. *Construction and Building Materials*, 276:122249. https://doi.org/10.1016/j.conbuildmat.2021.122249

Maich AA, Gronsky R, Komvopoulos K, 2024. Microstructure evolution and fretting wear mechanisms of steels undergoing oscillatory sliding contact in dry atmosphere. *Materials*, 17(8):1737. https://doi.org/10.3390/ma17081737

Nejad RM, Shariati M, Farhangdoost K, 2016. Effect of wear on rolling contact fatigue crack growth in rails. *Tribology International*, 94:118-125. https://doi.org/10.1016/j.triboint.2015.08.035

Pereira HB, Echeverri EAA, Alves LHD, et al., 2024. Influence of HAZ microstructure on RCF under twin-disc test of a flash-butt welded rail. *Wear*, 546-547:205324. https://doi.org/10.1016/j.wear.2024.205324

Remes H, Gallo P, Jelovica J, et al., 2020. Fatigue strength modelling of high-performing welded joints. *International Journal of Fatigue*, 135:105555. https://doi.org/10.1016/j.ijfatigue.2020.105555

Sallaba F, Rolof F, Ehlers S, et al., 2022. Relation between the fatigue and fracture ductile-brittle transition in S500 welded steel joints. *Metals*, 12(3):385. https://doi.org/10.3390/met12030385

Seo JW, Jun HK, Kwon SJ, et al., 2016. Rolling contact fatigue and wear of two different rail steels under rolling–sliding contact. *International Journal of Fatigue*, 83:184-194. https://doi.org/10.1016/j.ijfatigue.2015.10.012

Shen MX, Li JQ, Li L, et al., 2024. Adhesion and damage behaviour of wheel–rail rolling–sliding contact suffering intermittent airflow with different humidities and ambient temperatures. *Tribology Letters*, 72(1):18. https://doi.org/10.1007/s11249-023-01817-1

Shi HC, Shi LB, Ding HH, et al., 2019. Influence of laser strengthening techniques on anti-wear and anti-fatigue properties of rail welding joint. *Engineering Failure Analysis*, 101:72-85. https://doi.org/10.1016/j.engfailanal.2019.03.012

Tabaie S, Rézaï-Aria F, Flipo BCD, et al., 2021. Grain size and misorientation evolution in linear friction welding of additively manufactured IN718 to forged superalloy AD730™. *Materials Characterization*, 171:110766. https://doi.org/10.1016/j.matchar.2020.110766

Tan JH, Gao ZK, Ren S, et al., 2024. Improving the microstructures and mechanical properties of U71Mn rail steel liner friction welded joint by normalizing treatment. *Materials Today Communications*, 38:107736. https://doi.org/10.1016/j.mtcomm.2023.107736

Wang CS, Wu B, Hang W, et al., 2024. Precise surface machining of fused silica using high stability atmospheric pressure microwave plasma jet with a new internal electrode. *Surfaces and Interfaces*, 49:104379. https://doi.org/10.1016/j.surfin.2024.104379

Wang K, Ma QT, Xu JM, et al., 2022. Theoretical study of laminar plasma quenching of rail steel using the fluid-solid-thermal coupling method. *International Journal of Thermal Sciences*, 179:107708. https://doi.org/10.1016/j.ijthermalsci.2022.107708

Wang K, Lai J, Xu JM, et al., 2023a. Multiscale analysis of wheel-rail rolling contact wear and damage mechanisms using molecular dynamics and explicit finite elements. *Tribology International*, 185:108574. https://doi.org/10.1016/j.triboint.2023.108574

Wang K, Bai TS, Xu JM, et al., 2023b. Surface treatment of rail to enhance rolling contact fatigue and wear resistance: combined spot laminar plasma quenching and tempering method. *Construction and Building Materials*, 401:132832. https://doi.org/10.1016/j.conbuildmat.2023.132832

Wang K, Bai TS, Xu JM, et al., 2024a. Analysis of rolling contact fatigue and wear characteristics of aging-treated laminar plasma strip quenching rails. *Wear*, 540-541:205245. https://doi.org/10.1016/j.wear.2024.205245

Wang K, Bai TS, Xu JM, et al., 2024b. Investigation into the mechanisms of corrosion-induced rolling contact fatigue crack initiation and propagation in pearlitic rails. *Engineering Failure Analysis*, 163:108614.

https://doi.org/10.1016/j.engfailanal.2024.108614

Wang K, Yang J, Tian CX, et al., 2025. Study on gradient microstructural characteristics and crack propagation mechanisms in plasma-quenched rails and white etching layer containing rails. *Tribology International*, 211:110864.
https://doi.org/10.1016/j.triboint.2025.110864

Xu JM, Wang K, Zhang RH, et al., 2020. An investigation into the microstructure and tribological properties of rail materials with plasma selective quenching. *Tribology International*, 146:106032.
https://doi.org/10.1016/j.triboint.2019.106032

Xu JM, Wang K, Liang XY, et al., 2021. Investigation on wear and damage characteristics of high-speed rail steel with plasma selective quenching. *Wear*, 486-487:204100.
https://doi.org/10.1016/j.wear.2021.204100

Zeng DF, Lu LT, Gong YH, et al., 2017. Influence of solid solution strengthening on spalling behavior of railway wheel steel. *Wear*, 372-373:158-168.
https://doi.org/10.1016/j.wear.2016.12.025

Zhang SY, Liu QY, Wang WJ, et al., 2022. Implications of water medium for the evolution of rolling contact fatigue under rail surface defect conditions. *Tribology International*, 175:107870.
https://doi.org/10.1016/j.triboint.2022.107870

Zhao JZ, Miao HC, Kan QH, et al., 2021. Numerical investigation on the rolling contact wear and fatigue of laser dispersed quenched U71Mn rail. *International Journal of Fatigue*, 143:106010.
https://doi.org/10.1016/j.ijfatigue.2020.106010

Zhao P, Liu Z, Du F, et al., 2018. Ultra-high cycle fatigue property of a multiphase steel microalloyed with niobium. *Materials Science and Engineering: A*, 718:1-8.
https://doi.org/10.1016/j.msea.2018.01.085

Zhao P, Xu Z, Wang M, et al., 2021. High cycle fatigue behavior and microstructure of a high-speed rail material. *Materials Science and Engineering: A*, 824:141804.
https://doi.org/10.1016/j.msea.2021.141804

Zhu H, Bai TS, Shen BR, et al., 2024. An investigation into crack initiation and extension mechanism of laminar plasma quenched-tempered rail material with different quenched zones. *Tribology International*, 199:109983.
https://doi.org/10.1016/j.triboint.2024.109983

Zhu H, Bai TS, Xu JM, et al., 2025. Surface treatment of rail welded joints to balance wear in different zones: laminar plasma inhomogeneous quenching method. *Wear*, 580-581:206236.
https://doi.org/10.1016/j.wear.2025.206236

Electronic supplementary materials

Section S1, Tables S1–S3, Figs. S1–S7